

Charge Density Distributions, Interaction Energies, and Electrostatic Potentials of Hydrogen Bonds

Kuan-Jiuh Lin, Ming-Chu Cheng, and Yu Wang*

Department of Chemistry, National Taiwan University, Taipei, Taiwan, Republic of China

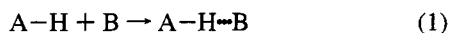
Received: May 10, 1994; In Final Form: August 29, 1994[®]

A hydrogen bond study was performed on dimethylammonium hydrobis(squarate), $(\text{H}_2\text{NMe}_2)^+[\text{H}(\text{HC}_4\text{O}_4)_2]^-$, using a detailed electron density distribution from accurate X-ray diffraction and ab initio molecular orbital calculations. The interaction energy between two H-bonded fragments and the electrostatic potential through the H-bond were also investigated. The anion of this compound contains both a symmetric ($\text{O}\cdots\text{H}\cdots\text{O}$ distance of 2.4321(8) Å, bond angle of 179(2)°) and an asymmetric ($\text{O}\cdots\text{H}\cdots\text{O}$ distance of 2.5645(6) Å, bond angle of 175(1)°) H-bond in the crystal. The compound crystallizes in the orthorhombic space group *Pccn*. The cell parameters at 136(1) K are $a = 15.614(3)$ Å, $b = 6.0537(7)$ Å, $c = 11.691(2)$ Å, and $Z = 4$. Deformation density distributions are illustrated in terms of $\Delta\rho_{\text{X-X}}$, $\Delta\rho_{\text{M-A}}$, and $\Delta\rho_{\text{theo}}$; the former two are calculated from experimental data with the spherical and multipole atomic model, respectively, and the last one is derived from the ab initio calculation using a 3-21+G** basis set with the geometry obtained from the crystal structure. All these deformation density distributions give consistent agreement. The ring strain of the four-membered squarate ring is nicely demonstrated in the deformation density map with the bonding electron density maximum outward from the C–C interatomic axis (exocyclic), such that two neighboring bonding electron density maxima give an angle of 110° around C2, which is much larger than the corresponding C1–C2–C3 angle of 90.83(4)°. Both the symmetric and asymmetric H-bonds are illustrated in the deformation density maps; their differences are quite observable. The interaction energies of both types of H-bond are calculated; their values after basis set superposition error (BSSE) correction are –54.4 and –19.9 kcal/mol for symmetric and asymmetric, respectively. According to natural bond orbital (NBO) analysis, the charge transfer energy and/or the mutual polarization do play an important role in stabilizing the linear hydrogen-bonding system. A differential molecular electrostatic potential (DMEP) study demonstrates such charge transfer phenomena and gives a quantitative description about the potential well along the O–O line of the H-bonds.

Introduction

In many organic and biological systems, the carboxyl group is the most common base to form a hydrogen bond with a proton donor such as an OH or NH group. Many studies have been published concerning the structure,^{1–3,19} bonding character,^{4–18} and spectroscopic properties^{14–16} of the H-bond. Conventionally, X-ray diffraction of a crystal provides information on the electron density of the crystal. Chemical bonding information may be derived from deformation electron density studies;^{19–21} hydrogen bonding was previously observed in such studies.^{22,23,45}

In general, we write a hydrogen-bonding species as $\text{A}\cdots\text{H}\cdots\text{B}$, where A–H represents a molecular fragment and B is a Lewis base, i.e. σ and/or π electron donor. Thus, decomposing the hydrogen bonding into two fragment is proposed as in eq 1, which is the same as the one used for the other intermolecular complexes such as donor–acceptor complexes. The interaction energy, ΔE_{int} , is defined as the difference between the energy of the system ($\text{A}\cdots\text{H}\cdots\text{B}$) and the sum of the energies of two fragments, A–H and B, as in eq 2.



$$\Delta E_{\text{int}} = E_{\text{A}\cdots\text{H}\cdots\text{B}} - (E_{\text{A}\cdots\text{H}} + E_{\text{B}}) \quad (2)$$

$$\Delta E_{\text{int}}(\text{SCF}) = E_{\text{el}} + E_{\text{pl}} + E_{\text{ex}} + E_{\text{CT}} + E_{\text{mix}} \quad (3)$$

The interaction energy, ΔE_{int} , derived at the ab initio SCF level is composed of several terms known as energy decomposi-

tion analysis shown in eq 3. This was initially proposed by Morokuma and Kitaura,^{24,25} where E_{el} is an electrostatic energy term representing the interaction between two fragments with respective unperturbed charge distributions. E_{pl} is a polarization energy term representing the energy associated with the charge polarization in B in the presence of the electron field of A–H and vice versa. E_{ex} is an exchange repulsion term representing the Pauli exclusion energy between the electrons in fragment A–H and those in B. E_{CT} is a charge transfer term representing the energy of electron transfer from one fragment to the other. E_{mix} is defined as the difference between the total interaction energy and the sum of the four leading terms. Among these energy terms, the electrostatic energy is in general the dominant term of the interaction energy;²⁶ for instance in this work, the order of magnitude of E_{el} is equal to the order of magnitude of the binding energy. But this does not mean that E_{el} is the only factor responsible for the stability of the H-bonded complexes. The charge transfer energy (E_{CT}) and the polarization energy (E_{pl}) become crucial for the stabilization of H-bonded complexes when the filled (n) and unfilled (σ^*) orbitals are taken into account.^{27,28}

Net atomic charge can provide a simple and intuitive way to rationalize the chemical reactivity. However, it has been seriously criticized, since it is not a well defined physical property.^{30,32} It must be evaluated by means of appropriate partitioning of the charge distribution. One widely used method for partitioning is Mulliken population analysis (MPA),²⁹ but its shortcoming in overestimating the net atomic charge is well-known.^{27,30,31,38} Another recently widely adopted partitioning method is natural population analysis (NPA);^{27,30} it overcomes

* To whom correspondence should be addressed.

[®] Abstract published in *Advance ACS Abstracts*, October 15, 1994.

TABLE 1: Crystal Data of (H₂NMe₂)⁺[H(C₄O₄)₂]⁻ at 136(1) K

formula	(H ₂ NMe ₂) ⁺ [H ₃ (C ₄ O ₄) ₂] ⁻
temp (K)	136
space group	<i>Pccn</i>
<i>a</i> (Å)	15.614(3)
<i>b</i> (Å)	6.0537(7)
<i>c</i> (Å)	11.691(2)
volume (Å ³)	1105.0(3)
no. of cell para. detn	25
2θ range for cell para. detn	20.98–49.38
<i>Z</i>	4
<i>D</i> _{cal} (g cm ⁻³)	1.642
color	colorless
<i>F</i> (000)	568
Mo Kα (Å)	0.710 69
crystal size (mm ³)	0.70 × 0.52 × 0.25
absorp coeff (cm ⁻¹)	14.0
transmission coeff	0.93–0.97
θ/2θ scan parameter	2(0.80 + 0.35 tan θ)
2θ max. (deg)	100
<i>h</i> , <i>k</i> , <i>l</i> range	0–33, 0–13, 0–25
no. of reflns measured	33013
no. of unique reflns	5713
no. of obs reflns (<i>I</i> > 2.0σ)	3715
Σ(<i>I</i> _i - ⟨ <i>I</i> ⟩)/Σ <i>I</i> (%)	2.1
<i>R</i> _w ^a , <i>R</i> _w ^b	0.040; 0.045
<i>R</i> _w ^a , <i>R</i> _w ^b (sin θ/λ ≥ 0.70)	0.041; 0.033
weight modifier, <i>c</i> <i>f</i>	0.0001
<i>S</i> ^d	2.41
secondary extinction coeff	2.58 × 10 ⁻⁵

^a *R* = Σ(*F*_o - *F*_c)/Σ*F*_o. ^b *R*_w = [(Σ*w*(*F*_o - *F*_c)²)/(Σ*wF*_o²)^{1/2}]. ^c *w* = 1/[σ²(*F*_o) + *fF*_o²]. ^d (Goodness of fit, *S* = [(Σ*w*(*F*_o - *F*_c)²)/(*N*_{obs} - *N*_{var})]^{1/2}; *N*_{obs}, no. of observed reflections; *N*_{var}, no. of variables.

some deficiencies found in the MPA. Such analysis has been applied to a variety of chemical systems and has produced very promising results.^{27,30,31,32}

Electrostatic potential²⁵ is used to correlate the long-range chemical reactivity, especially to predict the protonation site. Such potential may give some insight about H-bonds.

With all this background in H-bond studies, the title compound, dimethylammonium hydrobis(squarate), was chosen for several reasons: (1) It contains a very strong symmetric H-bond and a medium strong asymmetric H-bond in the same compound. (2) It contains an interesting four-membered ring; the "bent" bond of such a small ring could be investigated through electron density distribution. (3) The interaction energies of both H-bond types can be analyzed according to the fragment decomposition technique; whether the electrostatic potential or charge transfer is more important in such system can be realized. (4) Net atomic charges of such a compound can provide the evidence of charge transfer and/or polarization between two H-bonded fragments. (5) Finally, the electrostatic potential derivation of such a compound will provide the types of potential well concerning H-bonds.

Experimental Section

Data Collection and Refinements. The crystal of the title compound was obtained by diffusing benzene into the mix solution of squaric acid (3,4-dihydroxy-3-cyclobutene-1,2-dione) and *N,N*-dimethylacetamide.¹ There is apparently a phase transition at 110 K, and the cell parameters become too large to handle at lower temperature. Thus, the data were measured at 136 K, where the structure is the same as that at room temperature. The crystal data and some details of the experimental conditions are listed in Table 1. The intensity data were measured at 136 K on a CAD4 diffractometer equipped with a liquid N₂ gas-flow device. Mo Kα radiation was used for the measurement. Three equivalent sets of reflections (*hkl*, $\bar{h}\bar{k}l$, $\bar{h}kl$) were measured up to a 2θ value of 100°, and five more

equivalent sets of reflections ($\bar{h}kl$, $\bar{h}\bar{k}l$, $h\bar{k}l$, hkl , $\bar{h}k\bar{l}$) were measured up to a 2θ value of 60°. In addition, intensities at four ψ angles (-30°, -10°, 10°, 30°) were collected for each reflection of (*hkl*) up to a 2θ value of 60°. This yielded a total of 33 013 measurements, which gave 5713 unique reflections after averaging of all equivalents. An absorption correction was applied (before the averaging) according to six measured faces, the correctness of the face was checked against the experimental ψ curves of three reflections. The interset agreement is 2.1%. Normal least-squares refinement based on *F*_o was performed, the counting statistic weight was applied, and the standard deviation of the average intensity was taken as a geometric mean of all the σ's of equivalents. Reflections with *I* > 2σ(*I*) were considered observed and were used in the least-squares refinement. All six hydrogen atoms were located in the difference Fourier synthesis after several cycles of least-squares refinement.

Deformation Density. *X-X Deformation Density* (Δ*Q*_{X-X}). The deformation density (Δ*Q*) is defined as the difference between the molecular density and the promolecular density.²¹ The promolecular density is composed of the sum of the densities from the superposition of spherical free atoms, each centered at its equilibrium position of the molecule. The X-X deformation density is calculated as the difference between the observed density, *Q*_{obs}, and the promolecular density, which is the superposition of the sum of spherically averaged free atomic density, Σ*Q*_c. In order to obtain all the non-H atomic parameters for the promolecular density calculation, a high-order refinement (sin θ/λ ≥ 0.7 Å⁻¹; 2298 reflections) was carried out. The positional and thermal parameters of H atoms in the anion were fixed during the high-order refinement; the hydrogen positions of the dimethylammonium cation were displaced along the N-H vector to make the N-H distance of 1.0 Å in the high-order refinements. Fourier coefficients of (Δ*Q*_{X-X}) were taken to be the difference between *kF*_o and *F*_c, where *F*_c was calculated with the parameters obtained from high-order refinement and the scale factor *k* is the optimum scale in the data range of Fourier summation (sin θ/λ ≤ 1.08 Å⁻¹) with the coefficients *F*_c obtained from high-order refinement.

Multipole Model Deformation Density (Δ*Q*_{M-A}). The model deformation density distributions are generated by subtracting the spherical atomic electron density part from the atomic electron density evaluated according to a multipole model (eq 4).³⁴

$$Q_{\text{atomic}}(r) = P_c Q_{\text{core}} + P_v \kappa^3 Q_{\text{valence}}(\kappa r) + \sum_{l=0}^1 R_l(r) \sum_{m=-l}^l P_{lm} y_{lm} \quad (4)$$

$$R_l(r) = \frac{\zeta_l^{n_l+3}}{(n_l+2)!} r^{n_l} \exp(-\zeta_l r)$$

The first two terms are the spherical part of the atomic electron density, and the third term is the sum of multipole terms which are expressed as spherical harmonic functions (*y*_{lm}); *R*_l(*r*) is the radial distribution, and *n*_l and ζ_l are the parameters of the radial function. The coefficients (*P*_v, *P*_{lm}) of the multipole terms together with the atomic positions and thermal parameters are obtained from a full-matrix least-squares process based on the structure amplitudes (*F*_o) from X-ray diffraction data. The model deformation density distribution (Δ*Q*_{M-A}) is generated by subtracting the spherical parts (with *P*_v fixed at the value of a neutral atom) from the multipole atomic model.

Deformation density based on multipole refinement is calculated with a multipole expansion of the valence shell up to hexadecapoles for N, C, and O atoms and up to dipoles for H atoms. Hartree-Fock functions are used for the monopoles.

The multipole coefficients (P_{lm}) of the H atoms of each methyl group are constrained to be the same. The valence electron configurations of C, N, and O atoms are s^2p^2 , s^2p^3 , and s^2p^4 , respectively. Therefore, the model deformation density ($\Delta\rho_{M-A}$) is evaluated with Fourier coefficients up to the experimental data resolution $\sin \theta/\lambda \leq 1.08 \text{ \AA}^{-1}$, including 5713 reflections. The static model deformation map ($\Delta\rho_{M-A, \text{static}}$) does not include the nuclear vibration and is based on the Fourier summation up to the limiting sphere of Mo K α radiation $\sin \theta/\lambda \leq 1.41 \text{ \AA}^{-1}$ with 12 970 reflections.

All atomic scattering factor tables of both core and valence electrons are taken from *International Tables for X-ray Crystallography*.³³ All the computations are carried out on a MicroVax3800 using NRCVAX⁵¹ and MOLLY³⁴ programs for conventional and multipole refinement, respectively.

Theoretical Deformation Density. Our previous work³⁶ on small molecules concluded that the split valence 3-21G* basis set is the most economic but adequate basis function in calculating the deformation density distribution. Thus, the theoretical deformation density distribution is carried out at the RHF-SCF-MO level with the 3-21+G** basis set using the Gaussian92 program.³⁵ The theoretical deformation density is defined as the difference between the total molecular density and the promolecular electron density. The total molecular density is calculated in a closed shell ground state molecule at the RHF level; each occupied molecular orbital is assigned to have two electrons. The promolecular electron density is the sum of the superposition of the spherical atomic electron density with atoms at the same equilibrium nuclear positions as in the molecular geometry. Such a geometry is taken from the X-ray diffraction data at 136 K. The spherical atomic density is calculated at the ROHF/GVB level; each outer degenerate valence orbital is assigned to have equal population, e.g. $2/3$ and $4/3$ for each p orbital of a carbon and an oxygen atom, respectively.

Computational Procedures of the Characterizations of H-Bonds. *Interaction Energies.* The interaction energies are measured at the HFSCF level as in eq 2. However, there is an increase in the magnitude of the interaction energy as a result of the unequal size of basis sets between the system and the subsystem, so the basis set superposition error (BSSE) has to be taken into account. Thus, the interaction energy ($\Delta E_{\text{int}}^{\text{corr}}$) corrected for the BSSE is indicated in eq 5

$$\Delta E_{\text{int}}^{\text{corr}} = E_{A-H-B} - (E_{A-H}^{A-H(B)} + E_B^{B(A-H)}) \quad (5)$$

where the energy of the subsystem, $E_B^{B(A-H)}$, is calculated with the basis set of the subsystem B and of the subsystem A-H. However, no electrons are employed for the orbitals of subsystem A-H; such orbitals are therefore called "ghost" orbitals.

Differential Electron Density. In order to investigate the specific change in electron density distribution due to H-bond formation, the differential electron density distribution, $\delta\rho_{\text{H-bond}}^{\text{corr}}$, along the H-bond is examined. $\delta\rho_{\text{H-bond}}^{\text{corr}}$ is obtained by subtracting the electron density of two fragments from that of the H-bonded complex, as indicated in eq 6.

$$\delta\rho_{\text{H-bond}}^{\text{corr}}(r) = \rho_{A-H-B}(r) - (\rho_{A-H}^{A-H(B)}(r) + \rho_B^{B(A-H)}(r)) \quad (6)$$

Molecular Electrostatic Potential (MEP). The molecular electrostatic potential, $V(r)$, is the rigorous quantum mechanical

expectation value of the operator r^{-1} ; its expression is shown in eq 7.

$$V(r) = \sum_A \frac{Z_A}{|R_A - r|} - \int \frac{\rho(r) dr}{|r - r|} \quad (7)$$

where Z_A is the positive charge at nucleus A, located at R_A , and $\rho(r)$ is the molecular electron density at r . With the LCAO-MO framework, eq 7 becomes eq 8

$$V(r) = \sum_A \frac{Z_A}{|R_A - r|} - \sum_{\mu} \sum_{\nu} P_{\mu\nu} \frac{\chi_{\mu}(r)\chi_{\nu}(r) dr}{|r - r|} \quad (8)$$

where $P_{\mu\nu}$ is the (μ, ν) element of the first-order density matrix and χ_{μ} denotes the atomic orbital. This means that the MEP can be calculated directly from the density function, which is the product of wave functions. The first sum gives the positive potential; the second sum gives the negative potential. Therefore the sign of $V(r)$ in any particular region depends on whether the contribution from the nuclei (first sum) or that from electron density (second sum) is greater. An electrophile will be attracted to the region where $V(r)$ is most negative (the local minimum). In general, the MEP has long been recognized as a reactivity index of long-range chemical interactions.³⁸⁻⁴⁴ In order to see such an effect on the electrostatic potential of H-bonded species, a differential MEP ($\delta V_{\text{H-bond}}^{\text{corr}}$) is generated by using ab initio RHF-SCF-MO wave functions (3-21+G**) according to eq 9

$$\delta V(r)_{\text{H-bond}}^{\text{corr}} = V(r)_{A-H-B} - (V(r)_{A-H}^{A-H(B)} + V(r)_B^{B(A-H)}) \quad (9)$$

where $V(r)_{A-H-B}$ is the electrostatic potential of the H-bonded species and $V(r)_{A-H}^{A-H(B)}$ and $V(r)_B^{B(A-H)}$ are those of two isolated fragments. The BSSE is also considered here.

All the electron density calculations were performed with the MOLOT³⁷ program, and the contour plotting of the deformation density maps was generated with a locally developed program. All MO computations were performed on the Micro-vax 3800 computer; the plots were produced with a DEC-LN03+ laser jet plotter.

Results

The final atomic coordinates and equivalent isotropic thermal parameters (B_{eq}) obtained from conventional, high-order, and multipole refinements are given in Table 2. The agreement indices at the various stages of expanding the multipole series are listed in Table 3. Figure 1 shows the packing of molecules in the unit cell. A twofold axis parallel to the c axis of the unit cell passes through the N atom of the dimethylammonium cation and through the H atom of the symmetric H-bond in the anion. The extended H-bond network of the hydrobis(squarate) anion is shown in Figure 2. The dihedral angles between two squarate planes are $28.96(2)^{\circ}$ and $0.01(3)^{\circ}$ for X/Y and X/Z, respectively. Thus two squarate anions connected via an asymmetric H-bond, X/Z, are coplanar; the two anions connected via a symmetric H-bond, X/Y, are not in the same plane. Moreover, in order to understand all the characterizations mentioned above, two types of H-bonds in this compound may be classified as follows:

Symmetric H-Bond

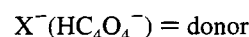
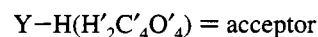
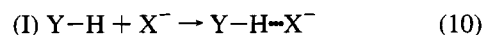


TABLE 2: Atomic Positional Parameters and B_{eq} Values (\AA^2)

		<i>x</i>	<i>y</i>	<i>z</i>	B_{eq}^d (\AA^2)
C2	<i>a</i>	0.119 42(3)	0.206 25(8)	0.338 70(4)	0.77(1)
	<i>b</i>	0.119 52(3)	0.206 19(7)	0.338 77(5)	0.76(1)
	<i>c</i>	0.119 56(2)	0.206 22(5)	0.338 76(3)	0.746(9)
C3	<i>a</i>	0.038 45(3)	0.119 16(8)	0.367 96(4)	0.75(1)
	<i>b</i>	0.038 38(3)	0.118 82(8)	0.367 92(4)	0.75(1)
	<i>c</i>	0.038 37(2)	0.118 79(6)	0.368 00(3)	0.735(9)
C4	<i>a</i>	0.000 09(3)	0.339 11(8)	0.378 65(5)	0.82(1)
	<i>b</i>	0.000 04(3)	0.338 98(7)	0.378 63(5)	0.82(1)
	<i>c</i>	0.000 03(2)	0.339 07(5)	0.378 68(3)	0.809(9)
C1	<i>a</i>	0.086 47(3)	0.431 71(8)	0.348 74(5)	0.79(1)
	<i>b</i>	0.086 48(3)	0.431 99(7)	0.348 71(4)	0.79(1)
	<i>c</i>	0.086 55(2)	0.432 11(6)	0.348 71(3)	0.769(9)
O2	<i>a</i>	0.191 32(3)	0.117 92(7)	0.312 03(4)	1.09(1)
	<i>b</i>	0.191 25(3)	0.117 94(7)	0.312 03(5)	1.07(1)
	<i>c</i>	0.191 22(2)	0.117 80(7)	0.311 99(4)	1.05(1)
O3	<i>a</i>	0.006 15(3)	-0.077 48(6)	0.378 44(4)	0.98(1)
	<i>b</i>	0.006 23(3)	-0.077 58(6)	0.378 28(4)	0.962(9)
	<i>c</i>	0.006 18(3)	-0.077 47(6)	0.378 27(4)	0.95(1)
O4	<i>a</i>	-0.070 78(3)	0.415 99(7)	0.397 56(4)	1.28(1)
	<i>b</i>	-0.070 74(3)	0.416 18(8)	0.397 40(6)	1.26(1)
	<i>c</i>	-0.070 77(3)	0.416 18(8)	0.397 48(5)	1.24(1)
O1	<i>a</i>	0.116 04(3)	0.619 58(6)	0.334 02(4)	1.06(1)
	<i>b</i>	0.116 06(3)	0.619 50(6)	0.333 97(5)	1.06(1)
	<i>c</i>	0.116 11(3)	0.619 42(6)	0.333 96(4)	1.04(1)
N	<i>a</i>	0.25	0.25	0.150 74(6)	1.20(2)
	<i>b</i>	0.25	0.25	0.150 91(7)	1.18(2)
	<i>c</i>	0.25	0.25	0.150 75(6)	1.17(2)
C5	<i>a</i>	0.220 47(4)	0.561 9(1)	0.079 95(6)	1.51(2)
	<i>b</i>	0.220 45(5)	0.562 1(1)	0.080 26(8)	1.50(2)
	<i>c</i>	0.220 42(3)	0.562 20(8)	0.080 37(4)	1.48(1)
H4	<i>a, b</i>	0.268 8(7)	0.497(2)	0.040(1)	2.7(2)
	<i>c</i>	0.274 37	0.489 2	0.035 95	1.9(2)
H5	<i>a, b</i>	0.199 7(7)	0.445(2)	0.131(1)	2.9(2)
	<i>c</i>	0.197 52	0.433 05	0.136 04	1.75(1)
H6	<i>a, b</i>	0.180 4(7)	0.613(2)	0.027(1)	2.9(2)
	<i>c</i>	0.173 92	0.621 46	0.018 99	1.90(2)
H3	<i>a, b</i>	0.291 0(6)	0.701(2)	0.193(1)	2.9(2)
	<i>c</i>	0.301 49	0.689 05	0.203 74	1.0(2)
H1	<i>a, b</i>	0.050 1(8)	-0.189(2)	0.364(1)	4.2(3)
	<i>c</i>	0.050 13	-0.189 27	0.364 27	0.9(2)
H2	<i>a, b</i>	0.25	0.25	0.312(2)	5.0(4)
	<i>c</i>	0.25	0.25	0.312 25	1.2(2)

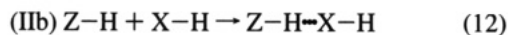
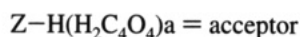
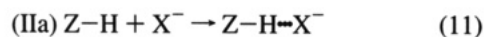
^a From full data refinement. ^b From high-order data ($\sin \theta/\lambda \geq 0.7$) refinement. ^c From multiplet refinement. ^d $B_{eq} = 8/3\pi^2 \sum_i U_{ij} a_i a_j^*$.

TABLE 3: Agreement Indices at Various Stages of Multipole Refinements

	variable	R_1^a	R_2^b	R_{1w}^c	R_{2w}^d	<i>S</i>
conventional	88	0.0592	0.0637	0.0614	0.0792	3.0188
monopole	105	0.0543	0.0544	0.0479	0.0621	2.3577
octapole	257	0.0417	0.0340	0.0254	0.0364	1.2735
hexadecapole	348	0.0401	0.0302	0.0233	0.0288	1.1788

^a $R_1 = \sum |F_o - kF_c| / \sum |F_o|$. ^b $R_2 = \sum |F_o^2 - kF_c^2| / \sum F_o^2$. ^c $R_{1w} = (\sum w|F_o - kF_c|^2 / \sum F_o^2)^{1/2}$. ^d $R_{2w} = (\sum w|F_o^2 - kF_c^2|^2 / \sum F_o^4)^{1/2}$.

Asymmetric H-Bond



The deformation density distribution at the plane of the squarate fragment with an asymmetric H-bond (X/Z) is shown in Figure 3. The deformation density distribution of the symmetric H-bond (X/Y) is shown in Figure 4. There are four maps each in Figures 3 and 4: namely, (a) $\Delta\rho_{X-X}$, (b) $\Delta\rho_{M-A}$, (c) $\Delta\rho_{M-A,static}$, (d) $\Delta\rho_{theo}$. The interaction energies for both symmetric and asymmetric H-bonds based on RHF-SCF cal-

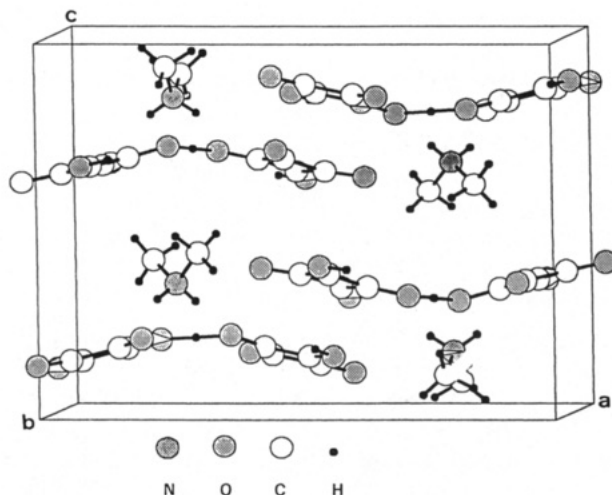
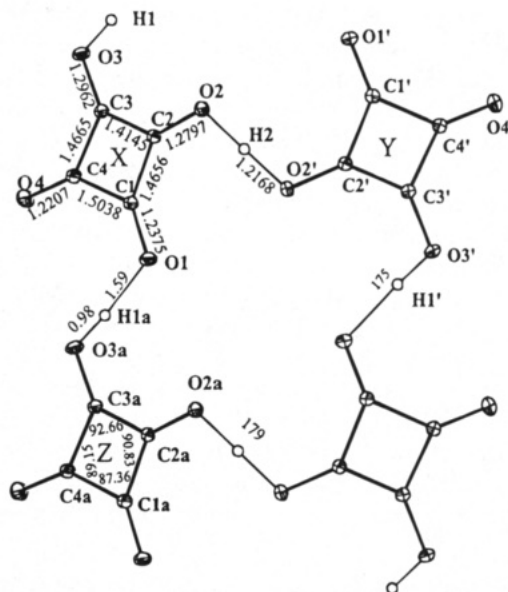
**Figure 1.** Molecular packing in the unit cell.

Figure 2. Extended H-bond network of the anion with 50% probability in thermal ellipsoids of non-H atoms. Selected bond lengths and bond angles from high-order refinement are given. X⁻ represents donor fragment (HC₄O₄⁻); Y-H and Z (H₂C₄O₄) are acceptor fragments for symmetric and asymmetric H-bonds, respectively. The deviations of C-C bond length, C-O bond length and C-C-C bond angle are 0.0007 Å, 0.0006 Å, and 0.04°, respectively.

culations are listed in Table 4. Net atomic charges obtained from the multipole refinement and from the MO calculation based on NPA are listed in Table 5. The charge transfer energies derived from the second-order perturbation energy, $\Delta E^2 = -2\langle n|F|\sigma^*\rangle^2/(\epsilon_n - \epsilon_{\sigma^*})$, where *F* is the Fock operator, are listed in Table 6. Differential electron densities for both hydrogen bond types are shown in Figure 6. Differential MEPs for the two types are depicted in Figure 8. In addition, differential electrostatic energies for the two types along the O-O region are shown in Figure 9.

Discussion

Deformation Density Distribution. Positive deformation densities are observed along the C-O, C-C, and O-H bonds and in the lone pair region of the oxygen atoms. The lone pair densities on oxygen atoms are more pronounced in $\Delta\rho_{M-A}$ than in $\Delta\rho_{X-X}$. Other features both in the experimental and model deformation maps ($\Delta\rho_{M-A}$, $\Delta\rho_{X-X}$) are in good agreement. Two types of H-bonds can be easily recognized in Figures 3 and 4 with the lone pair density of the oxygen atom polarized toward

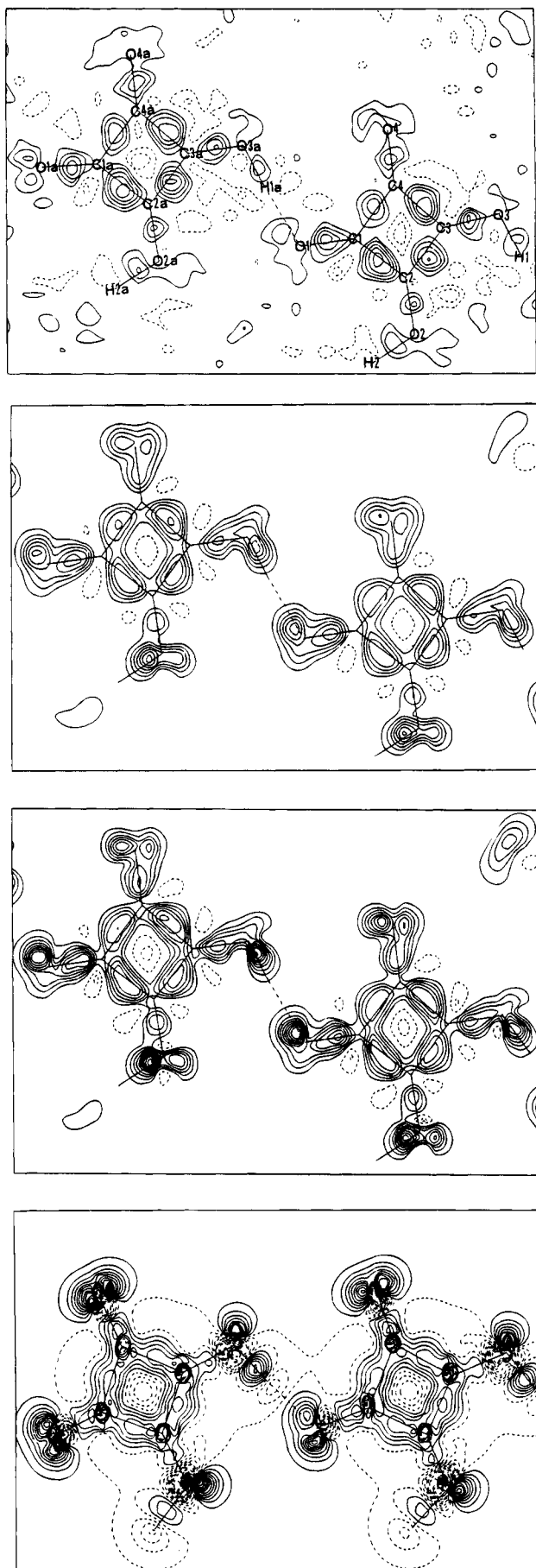


Figure 3. Deformation density distributions of anion ($\text{H}_3\text{C}_4\text{O}_4^-$) plane, X/Z, including asymmetric H-bond and the four-membered squarate ring. Contour interval is $0.1 \text{ e } \text{\AA}^{-3}$: solid line, positive; dotted line, negative; (a, top) $\Delta\rho_{\text{X-X}}$; (b, second from top) $\Delta\rho_{\text{M-A}}$; (c, third from top) $\Delta\rho_{\text{M-A,static}}$; (d, bottom) $\Delta\rho_{\text{theo,3-21+G**}}$.

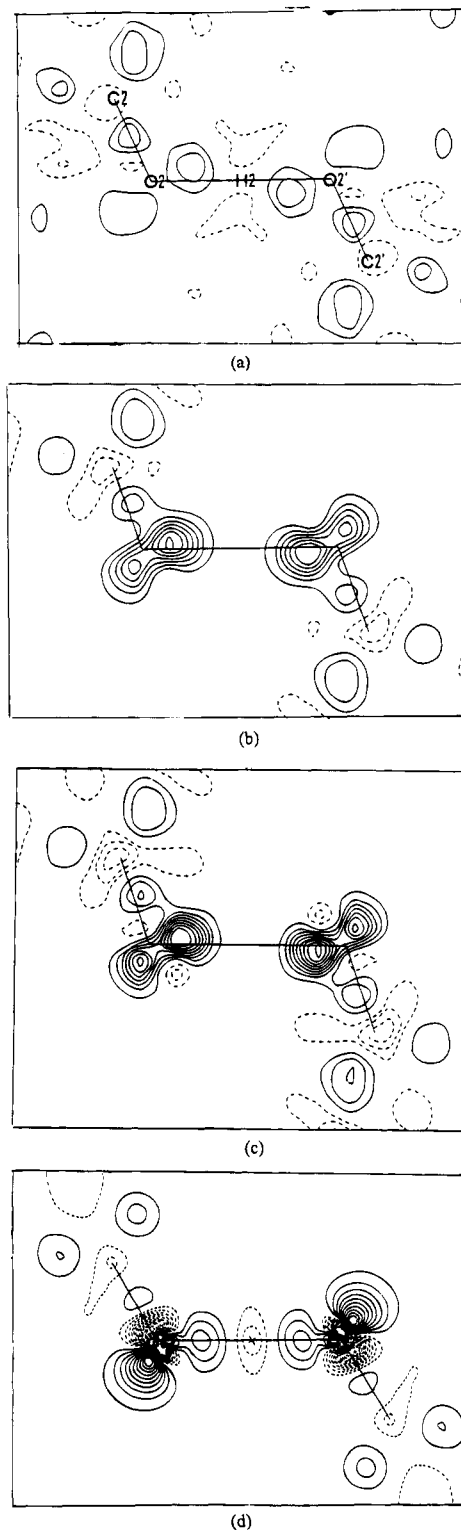


Figure 4. Deformation density distributions of symmetric H-bond at $\text{C}_2\text{-O}_2\text{-O}_2'$ plane. Contours as in Figure 3; a, b, c, and d as defined in Figure 3.

the hydrogen atom. The theoretical deformation density maps of $\text{H}_3(\text{C}_4\text{O}_4)_2^-$ using ab initio MO calculations with the 3-21+G** basis set shown in Figures 3d and 4d are quite comparable with the corresponding $\Delta\rho_{\text{M-A,static}}$. In comparison with the experimental deformation, $\Delta\rho_{\text{X-X}}$, the model deformation density distribution, $\Delta\rho_{\text{M-A}}$, not only shows clearer features but also enhances the density accumulation both along the bonds and at the lone pair regions. The geometry of the squarate fragment is clearly a 1,2-dione type with $\text{C}_2\text{-C}_3$ close to a double bond (1.415 \AA) and $\text{C}_1\text{-C}_4$ a single bond (1.504 \AA). $\text{C}_3\text{-C}_4$ and $\text{C}_1\text{-C}_2$ (1.466 \AA) are intermediate between a C-C

TABLE 4: Interaction Energies of Symmetric and Asymmetric H-Bonds Based on an HFSCF Calculation Using the 3-21+G Basis Set**

	r_{O-O} (Å)		E_{donor} (au)	E_{acceptor} (au)	E_{total} (au)	ΔE_{int} (kcal/mol)
symmetric	2.4325	I ^a	-449.056 10 ^b -449.060 83	-449.518 89 ^b -449.523 84	-898.671 40	-60.5 -54.4 ($\Delta E_{\text{int}}^{\text{corr}}$)
asymmetric	2.5648	IIa ^a	-449.060 29	-449.522 91	-898.614 91	-25.1 -19.9 ($\Delta E_{\text{int}}^{\text{corr}}$)
		IIb ^a	-449.1518 46	-449.523 78	-899.052 89	-9.5 -6.7 ($\Delta E_{\text{int}}^{\text{corr}}$)

^a Definitions of I, IIa, and IIb are according to eqs 10–12, where donor–acceptor fragments are given. ^b The respective energy without correction for BSSE.

TABLE 5: Net Atomic Charge, q , Derived from the Multipole Refinement and NPA

(a) Symmetric H-Bond (Y–H \cdots X [−])					
multipole	natural population (NPA)				Δq
	Y–H \cdots X [−]	q_{Y-H}	q_{X^-}		
C1'	+0.04(3)	+0.18	+0.26	0.00	−0.08
C2'	+0.03(3)	+0.31	+0.24	0.00	+0.08
C3'	0.02(3)	0.41	0.42	0.00	−0.01
C4'	+0.03(3)	+0.44	+0.45	0.00	−0.02
O1'	−0.25(2)	−0.68	−0.66	0.00	−0.02
O2'	−0.26(2)	−0.75	−0.66	0.00	−0.09
O3'	−0.29(2)	−0.56	−0.54	0.00	−0.02
O4'	−0.25(2)	−0.60	−0.51	0.00	−0.09
H1'	+0.26(2)	0.49	0.50	0.00	−0.01
H2	0.30(2)	0.53	+0.50	−0.01	+0.04
C1		+0.18	0.00	+0.11	+0.06
C2		+0.31	0.00	+0.32	+0.00
C3		+0.41	0.00	+0.41	+0.00
C4		+0.44	0.00	+0.41	+0.03
O1		−0.68	0.00	−0.69	+0.01
P2		−0.75	0.00	−0.74	−0.01
O3		−0.56	0.00	−0.60	+0.04
O4		−0.60	0.00	−0.66	+0.06
H1		+0.49	0.00	+0.47	+0.02

(b) Asymmetric H-Bond (Z–H \cdots X [−])				
	natural population (NPA)			Δq
	Z–H \cdots X [−]	q_{Z-H}	q_{X^-}	
C1	+0.49	−0.00	+0.46	+0.03
C2	+0.35	−0.00	+0.35	−0.00
C3	+0.20	−0.00	+0.15	+0.05
C4	+0.44	−0.00	+0.45	−0.01
O1	−0.72	−0.00	−0.67	−0.05
O2	−0.80	−0.00	−0.81	+0.01
O3	−0.74	−0.00	−0.75	+0.01
O4	−0.68	−0.00	−0.71	+0.03
H1	+0.54	−0.00	+0.53	+0.01
C1a	+0.45	+0.46	−0.00	−0.01
C2a	+0.25	+0.25	−0.00	−0.01
C3a	+0.32	+0.28	−0.00	+0.04
C4a	+0.49	+0.49	−0.00	−0.00
O3a	−0.73	−0.71	−0.00	−0.02
O1a	−0.67	−0.61	−0.00	−0.06
O2a	−0.72	−0.75	−0.00	0.03
O4a	−0.60	−0.56	−0.00	−0.04
H1a	+0.57	+0.55	−0.00	+0.02
H3a	+0.56	+0.59	−0.00	−0.03

TABLE 6: Charge Transfer Energies via NBO Based on HFSCF Calculation

basis set		$\langle n F \sigma^* \rangle$ (au)	$\epsilon_{\sigma^*} - \epsilon_n$ (au)	ΔE^2 (kcal/mol)	$q_{n \rightarrow \sigma^*}$
F-H \cdots F ⁻	HF/6-311+G**	0.493	1.35	225.6	0.27
I (symm)	HF/6-311+G**	0.425	1.06	211.1	0.33
I (symm)	HF/3-21+G**	0.422	1.12	197.0	0.28
IIa (asymm)	HF/3-21+G**	0.210	1.20	45.1	0.06
IIb (asymm)	HF/3-21+G**	0.133	1.57	13.8	0.02

single and a C–C double bond. This is also manifested by a very insensitive broad absorption band of 850–1710 cm^{−1} in the FTIR spectrum, which indicates some degree of π delocal-

ization in such a four-membered ring system. The experimental deformation density along C2–C3 does appear to be slightly larger than those along C3–C4 and C1–C2, which are then somewhat larger than that along C1–C4 (Figure 3a), but the differences among the C–C densities are not so obvious in Δq_{M-A} and Δq_{theo} (Figure 3b–d). The peak maxima of C–O are 0.5 and 0.6 e Å^{−3} in the static model density (Figure 3c); these values are comparable to those found in NaHCOO (120 K).⁴⁵ The theoretical deformation density maps and model static maps depict well the C–O bonding characters; i.e., the order of density accumulation along C–O bonds is C4–O4, C1–O1 > C2–O2, C3–O3, which is consistent with the corresponding bond lengths (Figure 2).

It is interesting to notice that the electron density distribution in the squarate plane clearly demonstrates the ring strain of the four-membered ring. The analysis of Δq provides a basis for a quantitative description of this phenomenon: a “convex” or a “concave” bent bond⁴⁷ is expected for any small ring compound which contains less than five first row elements (e.g. C, N, O, etc.). In this work, the bonding electron density maxima are outward from the C–C interatomic axis (exocyclic) in the deformation density maps (Figure 3). Such a bent bond feature is much more pronounced in Δq_{M-A} (Figure 3b,c); for instance, it gives an angle of 110° between two bonding maxima at the carbon atom (C2), the corresponding bond angle $\angle C1-C2-C3$ being only 90.83(4)°. This indicates that a convex bent bond is in good agreement with our experimental observation. The actual MOs for describing such a four-membered system are made either by r-set (radially oriented sp² hybrid orbitals) or by t-set (tangentially oriented p orbitals) orbitals,^{46–48} which will give a convex or a concave bent bond, respectively (see Figure 5). Since it takes four p electrons (t-set) for the ring σ bond and this bond covers all four carbon atoms, it is best described as σ electron delocalization. The electron densities of the long pair regions around the carbonyl oxygen atoms are quite different: the lone pairs at O4 are expected to be sp² hybrid, and those at O1 and O2 are between sp³ and sp² hybrids. However, the lone pair densities at O1 and O2 are affected quite significantly by the H-bond in the solid. The theoretical electron density distribution accumulation at the lone pair region is always significantly larger than the corresponding experimental one, since the long pair electron density is mostly localized molecular orbitals^{20,21,49} and the spherical atomic promolecular model does not take the orbital hybridization^{20,21,49} into account, which leads to an increase in electron density at this region. Along the asymmetric H-bond, the lone pair density at O1 is quite different from that at O4, which is a sp² like pair density (a pure ketone oxygen); however, it is similar to those at O2 and at O3, where a significant amount of density is polarized toward the H atom. Such phenomena are observed only in Δq_{X-X} and Δq_{M-A} maps. A somewhat contrary result is found in the theoretical deformation density distribution, where the lone pair density at O1 has less density accumulation toward the H atom in comparison with the other lone pairs at this atom. This may be explained by the charge transfer ($n \rightarrow \sigma^*$) process

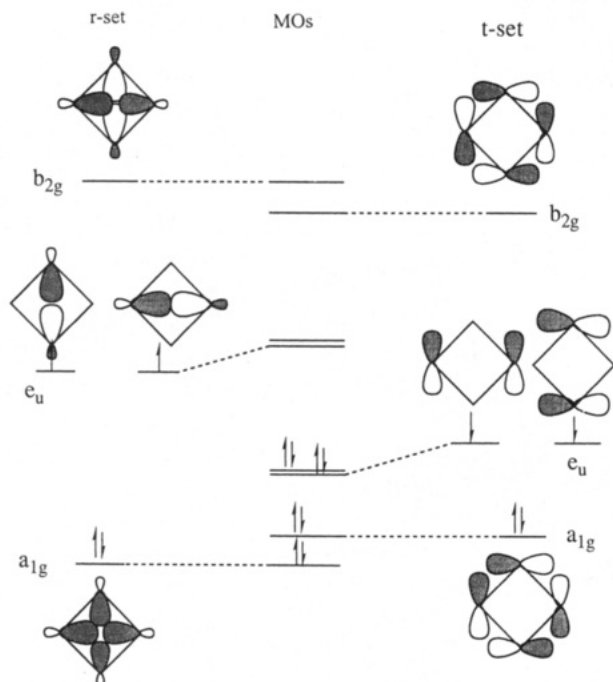


Figure 5. σ delocalizations of a four-membered ring based on simple Hückel theory. The r-set is composed of radially oriented orbitals, and the t-set is composed of tangentially oriented orbitals.⁴⁷

which will be discussed below. Along the symmetric H-bond, the O—H bond density is symmetrically distributed along the O—H—O line and the most probable sp^3 like lone pair is at O2. The agreement between the experimental and theoretical deformation density maps (Figure 4) is promising.

Characterizations of H-Bonds. *Interaction Energy.* According to the magnitude of the total interaction energy,⁵⁰ the H-bond may divide into weak, medium, and strong bonds, where the strong ones have ΔE_{int} of 20–60 kcal/mol and the short A—B, A—H distances of 2.2–2.5, 1.1–1.2 Å, respectively.

The corrected interaction energies ($\Delta E_{\text{int}}^{\text{corr}}$) of the two hydrogen bonds of this compound based on RHF-SCF calculations are shown in Table 4. They are −54.4 and −19.9 kcal/mol for the symmetric and asymmetric H-bond, respectively. The BSSE correction energies are 6.1 and 5.2 kcal/mol for the symmetric and asymmetric H-bond, respectively. This means that the BSSE is by no means a small fraction of the total energy; it reduces the interaction energy in this case by as much as 13% and 20% for the symmetric and asymmetric H-bond, respectively. The bond dissociation energy, which is the negative interaction energy, should be related to the energy of the hydrogen bond where the proton is shared evenly or unevenly between two fragments (X/Y or X/Z). It is apparent that the magnitude of such energy for the symmetric H-bond is almost at the same order of magnitude as that of a normal covalent bond. Our result for the symmetric H-bond energy is at the same magnitude as that of hydrobifluoride ion ($\text{F}=\text{H}=\text{F}$)[−] (60.2 kcal/mol).²⁷ Thus, such a symmetric H-bond should really be considered as an ionic H-bond and/or three-centered four-electron σ bond. Whereas the magnitude of the asymmetric one (ΔE_{IIa}) belongs to nearly strong H-bond, that of ΔE_{IIb} (neutral species) belongs to a medium H-bond. This indicates that the interaction energy is vastly affected by the ionic character of the donor fragment.

Charge Transfer. Differential electron density ($\delta\rho$) maps of H-bonds are shown in Figure 6a and b for symmetric and asymmetric H-bonds, respectively. It is interesting to note that, because of H-bond formation, the electron density is decreased around O2_{symm}, O1_{asymm} atoms of the donor fragment but is increased around O'2_{symm}, O3a_{asymm} atoms of the acceptor

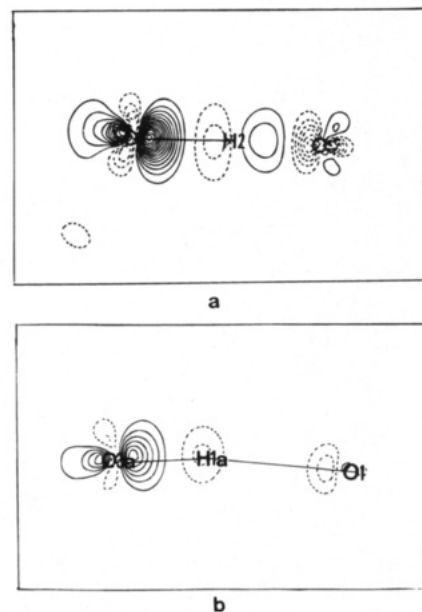


Figure 6. Differential electron density distribution of H-bonds based on an ab initio calculation using 3-21+G**; contours as in Figure 3: (a) for symmetric H-bond; (b) for asymmetric H-bond.

fragment. The amount of change in electron density is proportional to the H-bond strength, so that the change in the symmetric H-bond (Figure 6a) is significantly larger than that in the asymmetric H-bond (Figure 6b). Such a change is also correlated with the O—H bond length. This phenomenon can be understood as the outcome of an $n \rightarrow \sigma^*$ “charge transfer”. The charge is transferred from a lone pair orbital (n) of the O atom in the donor fragment to a $\sigma^*_{\text{O-H}}$ antibonding orbital of the acceptor fragment; the lengthening of the O—H bond is the result of such $\sigma^*_{\text{O-H}}$ character. Moreover, the charge transfer energies of $n \rightarrow \sigma^*_{\text{O-H}}$, listed in Table 5, are 197.0 and 45.1 kcal/mol for symmetric and asymmetric H-bonds, respectively. The amounts of charge transfer, $q_{n \rightarrow \sigma^*}$, are 0.28 and 0.06 e, respectively. In the case of the symmetric H-bond, the large charge transfer energy is at the same magnitude as that of hydrobifluoride ion (see Table 6). It therefore confirms the three-centered four-electron σ bond model shown in Figure 7. The charge transfer effect is also significant for the asymmetric H-bond in the case of IIa.

In addition to the differential molecular electron density distributions, the hydrogen bond strength can also be correlated with the Mulliken or natural population on H atoms (H2, H1a). The more positively charged an H atom is, the stronger the H-bond is.^{7,8} Table 5 gives the net atomic charges for the isolated fragments and the H-bonded species. The net atomic charge difference of the symmetric H2 atom (+0.04) is indeed more positive than that of the asymmetric H1a (+0.02). It is also noticed that, in the case of C—O—H—O (shown in Chart 1, both oxygen atoms involved in this hydrogen bonding become more negative and the C and H atoms become more positive than they are in the isolated fragments. This suggests that a mutual polarization has taken place during the H-bond formation. According to Bent's rule, the enhanced negative charge on the oxygen atom corresponds to the increase in p character of the lone pair on the donor oxygen atom in the direction of the H-bond; this would make the overlap between this non-bonding orbital n_O and the $\sigma^*_{\text{O-H}}$ antibonding orbital more effective. Thus, the net atomic charges of the donor oxygen atoms are −0.75 and 0.72 e for symmetric (O2) and asymmetric (O1), respectively. Again the lone pair electron density distributions of these oxygen atoms are polarized toward the H atom in the theoretical deformation maps shown in Figures 3d

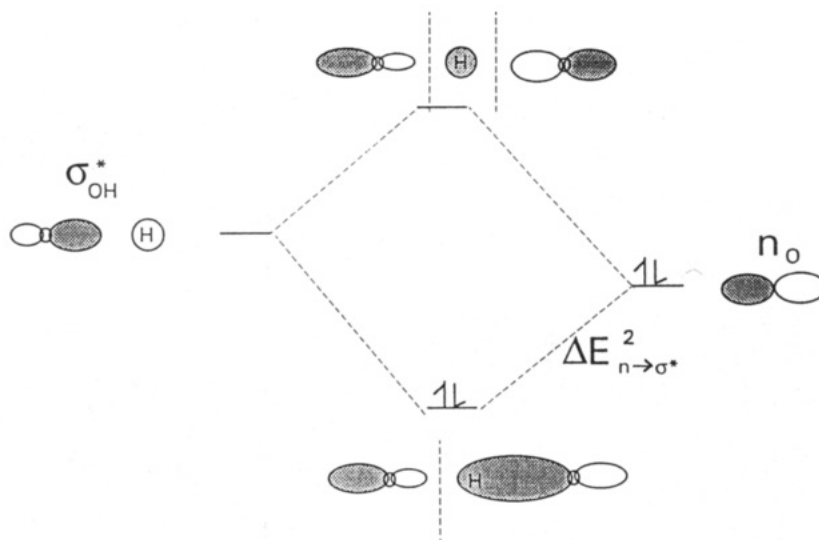


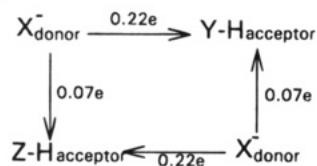
Figure 7. Charge transfer of H-bond, $n_O \rightarrow \sigma^*_{O-H}$ energy diagram.

CHART 1: Difference Net Atomic Charge Distribution (C-O-H-O) Due to H-Bond

	δ^+	δ^-	δ^+	δ^-	
	O2	H2	O2		I
	-0.09	+0.04	-0.01		
	-0.11	+0.18	-0.08		
NPA	+0.08				
MPA	+0.06				

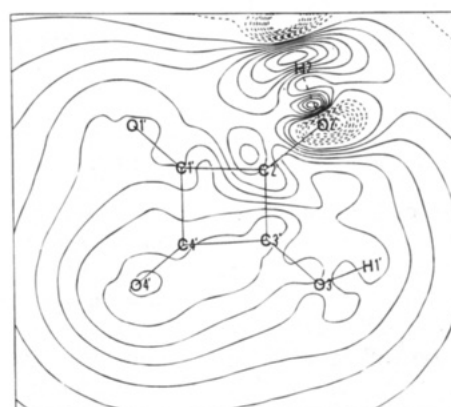
	δ^+	δ^-	δ^+	δ^-	
	O3a	H1a	O1		IIa
	-0.04	+0.02	-0.04		
	-0.05	+0.08	-0.09		
NPA	+0.02				
MPA	+0.03				

SCHEME 1: Charge Transfer from Donor Fragment to Acceptor Fragment via NPA

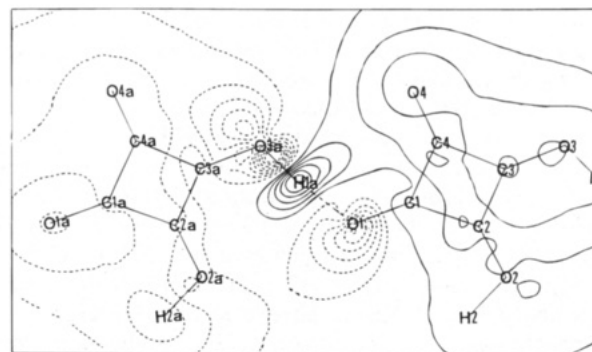


and 4d. The amounts of the net charge transfer (Table 5) from the donor fragment to the acceptor fragment are 0.22 and 0.07 e for symmetric and asymmetric H-bonds, respectively, as shown in Scheme 1.

Electrostatic Potential. Another interesting aspect of such an H-bond system is its effect on electrostatic potential distribution. The differential MEP maps for both H-bond types are shown in Figure 8. For the asymmetric H-bond (Figure 8b), it is obvious that a negative differential potential appears in the acceptor fragment (Z), except for the H1a atom, where it is positive. A positive differential potential appears in the donor fragment (X), except for the O1 atom, where it is negative. Such mutual polarization is consistent with the net atomic charge distribution (Chart 1) because both oxygen atoms (O3a, O1) reveal negative electrostatic potential. Bearing in mind that the less shielded the nucleus is, the more positive the potential is, the H1a nucleus must be poorly shielded; this is consistent with the high-field chemical shift on H-NMR. It is also worthwhile to point out that since there is a charge transfer from the donor fragment to the acceptor fragment, the loss in electron density of a donor fragment will give a positive differential MEP, but the gain in electron density of an acceptor fragment will give a negative differential MEP. This means that the electrostatic interaction energy of an H-bond between two fragments is incorporated with the charge transfer and/or polarization effect. The differential MEP of the symmetric H-bond case is presented



(a)



(b)

Figure 8. Differential electrostatic potential distribution. Contour interval $0.01 \text{ e } \text{\AA}^{-1} = -3.3 \text{ kcal/mol}$: (a) donor fragment of the symmetric H-bond; (b) asymmetric H-bond.

in Figure 8a; since the two fragments are not in the same plane, only one donor fragment is shown here. The general feature is the same as that of the asymmetric H-bond (Figure 8b); i.e., the donor fragment reveals a positive MEP except for the O2 atom (Figure 8a) and the acceptor fragment reveals a negative MEP except for the H2 atom. However, the charge transfer and/or mutual effects of the symmetric H-bond are much more apparent than that of the asymmetric one.

Furthermore, the features of the differential electrostatic potential along the O-H-O vector for both symmetric and asymmetric H-bonds are also shown in Figure 9. It is often thought that the proton should be going back-and-forth between the double minima (oxygen atoms) of the electrostatic potential

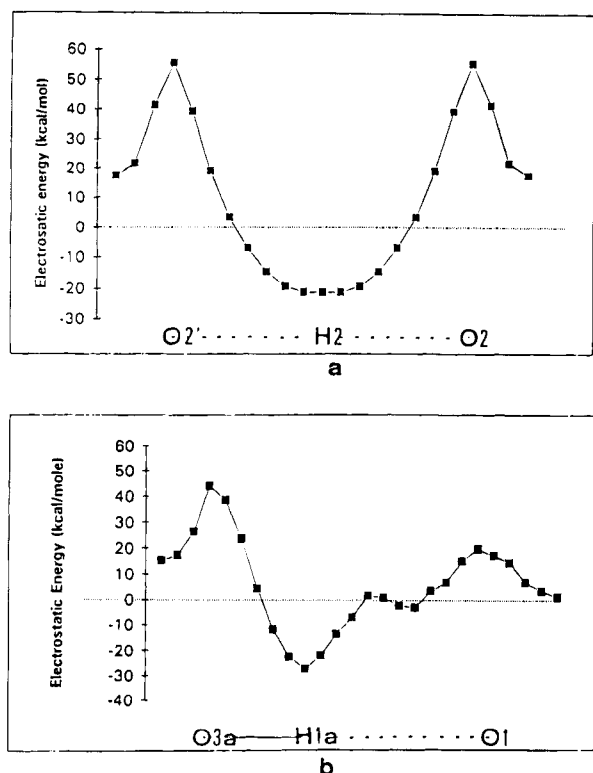


Figure 9. Electrostatic potential well along the O—O line for the (a) symmetric and (b) asymmetric H-bond.

well through tunneling and/or thermal motion.^{52,53} It is interesting to note that there is a single minimum in the case of the symmetric H-bond shown in Figure 9a, whereas there are double minima in the case of the asymmetric one shown in Figure 9b.

Conclusion

A deformation density study demonstrates that the electron density distribution of carbonyl oxygen lone pairs is between sp^3 and sp^2 hybrids due to H-bonds. A convex bent bond of the four-membered ring is illustrated. The symmetric and asymmetric H-bonds are analyzed on the basis of ab initio MO calculations. The symmetric H-bond is best described as a three-centered four-electron σ bond, whereas the asymmetric one is close to a strong dipole–dipole H-bond. The dominance of the charge transfer and/or mutual polarization effect is manifested in terms of the differential electron density, net atomic charge, and differential MEP results. A single minimum and double minima in the electrostatic potential well are found for symmetric and asymmetric H-bonds, respectively.

Acknowledgment. The authors would like to thank the National Science Council of the ROC for financial support.

Supplementary Material Available: Table SI, listing anisotropic temperature factors (U_{ij}) of all non-H atoms and U_{iso} of H atoms from various least-squares refinements, and Table SII, listing coefficients of atomic multipole population terms up to the hexadecapoles level for C, N, O atoms and up to dipoles for H atoms (4 pages); Table SIII, listing calculated and observed structure factors (21 pages). Ordering information is given on any current masthead page.

References and Notes

- (1) Wang, Y.; Stucky, G. D. *J. Chem. Soc., Perkin Trans. 2* **1974**, 925.
- (2) Macintyre, W. M.; Werkema, M. S. *J. Chem. Phys.* **1964**, *42*, 3563.
- (3) Hollander, F. J.; Semmingsen, D.; Koetzle, T. F. *J. Chem. Phys.* **1977**, *67*, 4825.
- (4) West, R.; Powell, D. L. *J. Am. Chem. Soc.* **1963**, *85*, 2577.
- (5) Ito, M.; West, R. *J. Am. Chem. Soc.* **1963**, *85*, 2580.
- (6) West, R.; Niu, H. Y.; Ito, M. *J. Am. Chem. Soc.* **1963**, *85*, 2584.
- (7) Reynolds, C. H. *J. Am. Chem. Soc.* **1990**, *112*, 7903.
- (8) Mirkin, N. G.; Krimm, S. *J. Am. Chem. Soc.* **1991**, *113*, 9742.
- (9) Vinson, L. K.; Dannenberg, J. J. *J. Am. Chem. Soc.* **1989**, *111*, 2777.
- (10) Shen, M.; Xie, Y.; Schaefer, H. F., III; Deakyne, C. A. *J. Chem. Phys.* **1990**, *93*, 3379.
- (11) Vedani, A.; Dunitz, J. D. *J. Am. Chem. Soc.* **1985**, *107*, 7653.
- (12) Murray-Rust, P.; Glusker, J. P. *J. Am. Chem. Soc.* **1984**, *106*, 1018.
- (13) Johansson, A.; Kollman, P.; Rothenberg, S.; McKelvey, J. *J. Am. Chem. Soc.* **1974**, *96*, 3794.
- (14) Gellman, S. H.; Adams, B. R.; Dado, G. P. *J. Am. Chem. Soc.* **1990**, *112*, 460.
- (15) Gellman, S. H.; Dado, G. P.; Liang, G. B.; Adams, B. R. *J. Am. Chem. Soc.* **1991**, *113*, 1164.
- (16) Novoa, J. J.; Whangbo, M. H. *J. Am. Chem. Soc.* **1991**, *113*, 9017.
- (17) Derrin, C. L.; Thoburn, J. D. *J. Am. Chem. Soc.* **1989**, *111*, 8010.
- (18) Kanters, J. A.; Schouten, A.; Kroon, J. *Acta Crystallogr.* **1991**, *C47*, 807.
- (19) Mensching, L.; Niessen, W. V.; Valtazanos, P.; Ruendenberg, K.; Schwarz, W. H. E. *J. Am. Chem. Soc.* **1989**, *111*, 6933.
- (20) Schwarz, W. H. E.; Ruendenberg, K.; Mensching, L. *J. Am. Chem. Soc.* **1989**, *111*, 6926.
- (21) Coppens, P.; Hall, M. B. *Electron Distribution and the Chemical Bond*; Plenum Press: New York, 1982.
- (22) Hermansson, K.; Tellgren, R. *Acta Crystallogr.* **1989**, *B45*, 252.
- (23) Wang, Y.; Tsai, C. J.; Liu, W. L. *Acta Crystallogr.* **1985**, *B41*, 131.
- (24) Kitaura, K.; Morokuma, K. *Int. J. Quantum Chem.* **1976**, *10*, 325.
- (25) Politze, P.; Truhlar, D. G. *Chemical Applications of Atomic and Molecular Electrostatic Potential*; Plenum Press: New York, 1981.
- (26) Umeyama, H.; Morokuma, K. *J. Am. Chem. Soc.* **1977**, *99*, 1316.
- (27) Reed, A. E.; Curtiss, L. A.; Weinhold, F. *Chem. Rev.* **1988**, *88*, 899.
- (28) Hobza, P.; Zahradnik, R. *Chem. Rev.* **1988**, *88*, 871.
- (29) Mulliken, R. S. *J. Chem. Phys.* **1962**, *36*, 3428.
- (30) Reed, A. E.; Weinstock, R. B.; Weinhold, F. *J. Chem. Phys.* **1985**, *83*, 735.
- (31) Orozco, M.; Luque, F. J. *J. Comput. Chem.* **1990**, *11*, 909.
- (32) Reed, A. E.; Schleyer, P. v. R. *J. Am. Chem. Soc.* **1990**, *112*, 1434.
- (33) *International Tables for X-ray Crystallography*; Kynock: Birmingham, England, 1974; (a) Vol. IV and (b) Vol. III, p 276.
- (34) Hansen, N. K.; Coppens, P. *Acta Crystallogr., Sect. A: Cryst. Phys., Diff., Theor. Gen. Crystallogr.* **1978**, *A34*, 909.
- (35) Frisch, M. J.; Trucks, G. W.; Head-Gordon, M.; Foresman, J. B.; Gill, M. W.; Wong, J. B.; Foresman, B. G.; Johnson, H. B.; Schlegel, H. B.; Robb, M. A.; Replogle, E. S.; Gomperts, R.; Andres, J. L.; Raghavachari, K.; Binkley, J. S.; Gonzalez, C.; Martin, R. L.; Defrees, D. J.; Fox, D. J.; Whiteside, R. A.; Seeger, R.; Melius, C. F.; Baker, J.; Stewart, J. J. P.; Pople, J. A. *Gaussian 92*, Revision A; Gaussian Inc.: Pittsburgh, PA, 1992.
- (36) (a) Lin, K. J.; Wang, C. C.; Wang, Y. *J. Chin. Chem. Soc.* **1991**, *38*, 505–512. (b) Lin, K. J.; Wang, Y. *J. Phys. Chem.* **1993**, *97*, 3176–3184.
- (37) Modified MOPLOT program (Lichtenberger, D. L.; Fenske, R. F. MOPLOT; Quantum Chemistry Program Exchange: 1975) to generate difference density distributions.
- (38) Lague, F. J.; Orozco, M.; Illas, F.; Rubio, J. *J. Am. Chem. Soc.* **1991**, *113*, 5203.
- (39) Faerman, C. H.; Sarah, L. P. *J. Am. Chem. Soc.* **1990**, *112*, 4915.
- (40) Stone, A. J. *Chem. Phys. Lett.* **1981**, *83*, 233.
- (41) Stone, A. J.; Alderton, M. *Mol. Phys.* **1985**, *56*, 1047.
- (42) Su, Z.; Coppens, P. *Acta Crystallogr.* **1992**, *A48*, 188.
- (43) Murray, J.; Lane, P.; Politzer, P. *Theochem* **1990**, *209*, 163.
- (44) Murray, J.; Redfern, P. C.; Lane, P.; Politzer, P. *Theochem* **1990**, *207*, 177.
- (45) Fuess, H.; Bats, J. W.; Dannohl, H.; Meyer, H.; Schweig, A. *Acta Crystallogr.* **1982**, *B38*, 736.
- (46) Dewar, M. J. S. *J. Am. Chem. Soc.* **1984**, *106*, 669.
- (47) Cremer, D.; Gauss, J. *J. Am. Chem. Soc.* **1986**, *108*, 7467.
- (48) Cremer, D. *Tetrahedron* **1988**, *44*, 7427.
- (49) Kunze, K. L.; Hall, M. B. *J. Am. Chem. Soc.* **1987**, *109*, 7617.
- (50) Kaplan, I. G. *Theory of Molecular Interactions*; Elsevier: New York, 1986.
- (51) Gabe, E. J.; LePage, Y.; Charland, J.-P.; Lee, F. L.; White, P. S. *J. Appl. Crystallogr.* **1989**, *22*, 384–387.
- (52) Moritomo, Y.; Koshihara, S.; Tokura, Y. *J. Chem. Phys.* **1988**, *93*, 5429.
- (53) Moritomo, Y.; Datsufuji, T.; Tokura, Y. *J. Chem. Phys.* **1991**, *95*, 2244.